Rudolph, S.; van der Kruk, J.; von Hebel, C.; Ali, M.; Herbst, M.; Montzka, C.; Patzold, S.; Robinson, D.A.; Vereecken, H.; Weihermuller, L.. 2015. **Linking satellite derived LAI patterns with subsoil heterogeneity using large-scale ground-based electromagnetic induction measurements.**

Linking satellite derived LAI patterns with subsoil heterogeneity using large-scale ground-based electromagnetic induction measurements

S. Rudolph[1,2], J. van der Kruk[1], C. von Hebel[1], M. Ali[1], M. Herbst[1], C. Montzka[1], S. Pätzold[3], D.A. Robinson[4], H. Vereecken[1] and L. Weihermüller[1]

[1]Forschungszentrum Jülich GmbH, Agrosphere Institute (IBG-3), Jülich, Germany
[2]now at the British Geological Survey, Environmental Science Centre, Keyworth, England (sebrud@bgs.ac.uk)
[3]University of Bonn, Institute of Crop Science and Resource Conservation (INRES), Division Soil Science, Bonn, Germany
[4]Centre for Ecology & Hydrology, Environment Centre Wales, Bangor, Wales

Keywords

Soil heterogeneity, combined sensor approach, electromagnetic induction *EMI*, leaf area index *LAI*, water holding capacity

Abstract

Patterns in crop development and yield are often directly related to lateral and vertical changes in soil texture causing changes in available water and resource supply for plant growth, especially under dry conditions. Relict geomorphologic features, such as old river channels covered by shallow sediments can challenge assumptions of uniformity in precision agriculture, subsurface hydrology, and crop modelling. Hence a better detection of these subsurface structures is of great interest. In this study, the origins of narrow and undulating leaf area index (*LAI*) patterns showing better crop performance in large scale multi-temporal satellite imagery were for the first time interpreted by proximal soil sensor data. A multi-receiver electromagnetic induction (*EMI*) sensor measuring soil apparent electrical conductivity (*ECa*) for six depths of exploration (*DOE*) ranging from 0-0.25 to 0-1.9 m was used as reconnaissance soil survey tool in combination with selected electrical resistivity tomography (*ERT*) transects, and ground truth texture data to investigate lateral and vertical changes of soil properties at ten arable fields. The moderate to excellent spatial consistency (R^2 0.19-0.82) of *ECa* patterns and *LAI* crop marks that indicate a higher water storage capacity as well as the increased correlations between large-offset *ECa* data and the subsoil clay content and soil profile depth, implies that along this buried paleo-river structure the subsoil is mainly responsible for better crop development in drought periods. Furthermore, observed stagnant water in the subsoil indicates that this paleo-river structure still plays an important role in subsurface hydrology. These insights should be considered and implemented in local hydrological as well as crop models.

1. Introduction

Spatial heterogeneity of subsurface properties such as soil texture, soil structure, as well as biochemical properties (e.g., organic carbon, nutrient status, pH) in combination with unfavorable climatic conditions are known to affect crop yield (De Benedetto et al., 2013). The detection, delineation, and quantification of subsurface variability are therefore key challenges for site-specific management and are essential for spatially resolved hydrological models and crop models.

Using grid sampling as a conventional soil survey technique is tedious and costly because a large set of soil samples is required to adequately describe field variability. To overcome these limitations, remotely sensed data obtained by active and passive sensors mounted on air-or spaceborne platforms have been used to extract information relevant for precision agriculture by delineating soil-patterns or segmenting the landscape into smaller but more homogenous regions.

In densely vegetated regions, spatial and temporal changes in spectral indices and biophysical attributes such as the normalized vegetation index (*NDVI*), soil adjusted vegetation index (*SAVI*), or the leaf area index (*LAI*) have been used to monitor crop growth and development, to map and classify crop vitality and yield production, and to detect early crop stress (Govender et al., 2009; Lelong et al., 1998; Lu, 2006; Zheng and Moskal, 2009). Additionally, soil properties and states characterizing the vadose zone such as soil texture, soil moisture, and water holding capacity were estimated successfully from spectral (Casa et al., 2013), thermal (Eisele et al., 2012), as well as from active (Zribi et al., 2012) and passive (Jonard et al., 2011) microwave remote sensing products. Unfortunately, spectral and thermal satellite remote sensing products do not include the ability to provide time critical remotely sensed observation, such as at night time or when cloud cover is present.

Although remote sensing appears to be an important and promising tool for precision agriculture it is not yet routinely used in plot scale agricultural soil science (Ben-Dor et al., 2009) due to low spatial and/or temporal resolution, the lack of real-time data (De Benedetto et al., 2013), and its limited sensitivity to mainly the upper few centimeters of the soil (Vereecken et al., 2008). Moreover, there are still many unsolved calibration and validation issues to relate remote sensing products with crop and soil properties due to the physically complex microwave interactions with soils at wavelengths of interest (Mohanty et al., 2013). Furthermore, remote sensing products analyzing crop water stress are restricted to observation periods where the crop stand shows substantial impact on the environmental conditions (Vereecken et al., 2012).

Despite these facts remote sensing can deliver important information, which can be used to improve and support the interpretation of existing soil data (McBratney et al., 2003) and help to set up spatially distributed hydrological and crop models.

To match the requirements of high-resolution mapping of the subsurface systems, non-invasive geo-referenced geophysical measurements with larger sensing depth are suggested that are capable of obtaining soil proxies that influence crop development. Hereby, different techniques are proposed such as electromagnetic induction (*EMI*) (Corwin, 2008; Corwin and Lesch, 2005), electrical resistivity tomography (*ERT*) (Besson et al., 2010; Samouelian et al., 2005), ground penetrating radar (*GPR*) (Huisman et al., 2003; Weihermüller et al., 2007), and gamma-ray spectrometry (Dierke and Werban, 2013). By measuring soil apparent electrical conductivity (*ECa*), soil electrical resistivity, soil dielectric permittivity, or concentration of gamma-ray emitting nuclides in soils, each sensor can be used to help determining specific soil properties, especially when used in combination.

Due to the easy handling and non-invasive measurements, *EMI* systems are the most frequently used proximal sensors in precision agriculture. The *EMI* system generates a time varying primary electromagnetic field in the transmitter coil, which induces a current into the subsurface (Hendrickx and Kachanoski, 2002; McNeill, 1980). A secondary magnetic field is generated by these currents and measured together with the primary magnetic field at the receiver coil. The ratio between the secondary and primary magnetic field is used to derive the soil apparent electrical conductivity, which depends on coil separation, coil orientation, operating frequency, and subsurface electrical conductivity. Due to the different soil properties influencing the subsurface electrical conductivity, a calibration of the measured geophysical signal is needed. In this way, *EMI* sensors can be used in various applications ranging from estimating the spatial variability of soil water content (Kachanoski et al., 1988; Robinson et al., 2012), clay content (Jung et al., 2005; Triantafilis and Lesch, 2005), and soil profile depth (Akbar et al., 2004; Saey et al., 2009). Recent developments of multi-receiver *EMI* systems enable the simultaneous *ECa* measurement for different depth ranges (Abdu et al., 2007; De Smedt et al., 2013; Saey et al., 2009). Additionally, inversion of these *EMI* data nowadays allows the *2D* (Mester et al., 2011; Triantafilis et al., 2011) or quasi-*3D* (Saey et al., 2012; von Hebel et al., 2014) characterization of the subsurface, which will improve the applicability of *EMI* for detailed large-scale subsurface studies.

With respect to the soil/vegetation continuum, geophysical and remote sensing techniques have different sensitivities and therefore, a combination of different proximal sensors and/or remote sensing data will enhance the data analysis and the understanding of the interactions between the subsurface and the vegetation as found by Robinson et al. (2010) for rangeland systems. This background also motivated Vereecken et al. (2008) in their review to recommend a combined use of geophysical measurements with remote sensing to estimate soil properties.

For example, several studies used a combination of *EMI* and *GPR* measurements to successfully estimate the spatial variability of soil properties (e.g. water content) and soil depth (De Benedetto et al., 2012; Jonard et al., 2013; Kruger et al., 2013). The effect of texture and fertilization on soil electrical conductivity was investigated by Lück et al. (2011), where *EMI* measurements were compared with inverted *ERT* transects. The study demonstrated that due to comparable sensitivities towards texture and soil water content, resistivity measurements could be used to explore the vertical variability of *ECa* with high resolution. The potential and limitations of a combined *EMI* and gamma-spectroscopy survey was demonstrated by Altdorff and Dietrich (2012) as well as Castrignanò et al. (2012) who showed that multivariate geostatistical techniques are essential to fuse data from the different sensors to delineate management or soil zones.

André et al. (2012) explored the potential of *EMI*, *GPR*, and *ERT* to delineate soil properties within a vineyard in France and to produce high-resolution soil stratigraphy maps. A comparison of these maps with *NDVI* data indicated anthropogenic soil compaction as a key factor controlling vine vigor problems. Similarly, De Benedetto et al. (2013) demonstrated that a combination of proximal and remote sensing is important for adequately describing soil properties and crop response. In addition, the capability of remotely derived vegetation indices to predict soil apparent electrical conductivity at large scales using multiple regression was investigated by Lausch et al. (2013). Their study demonstrated that vegetation indices derived from a reflectance spectrum between 420-800 nm in combination with terrain attributes could be used to characterize the crop stand and shallow *ECa* variability.

Most of the combined geophysical and remote sensing approaches use single-offset *EMI* systems that are not able to characterize subsurface property changes with depth. Here, we use multi-receiver *EMI* data, and large-scale multi-temporal and multispectral satellite imagery in conjunction with selected *ERT* transects and conventional soil sampling to investigate the influence of lateral and vertical changes in soil properties on the spatial and temporal variability of the crop performance of arable fields.

2. Materials and methods

2.1 Site description

The studied site comprises ten agricultural fields (in total 20 ha) at the TERENO (TERrestrial ENvironmental Observatories) site Selhausen (50°52'09''N 6°27'00''E), approximately 40 km west of Cologne, Germany. The climate is characterized by an average annual precipitation of 715 mm and a mean annual temperature of 10.2 °C.

The fields are cultivated in rotation with winter wheat, barley, and sugar beet but also potato, maize, oilseed rape and oat are grown occasionally. Additionally, one field (F10) is managed as bare soil (Weihermüller et al., 2007). All soils are developed in Quaternary sediments. The eastern part of the investigated area overlies the Upper Terrace (*UT*) that consists of Pleistocene sand and gravel sediments of the Rhine/Meuse river system and is characterized by a variety of shallow, narrow, and undulating subsurface channels, filled and buried by aeolian sediments with variable thickness (Klostermann, 1992; Pätzold et al., 2008; Vandenberghe and van Overmeeren, 1999). The fields in the western part overly the Lower Terrace (*LT*) that consists of Holocene fluvial deposits of the Rur river covered by floodplain deposits (>1.5 m) and loess (Röhrig, 1996). Translocation of soil material by soilfluction and soil erosion along a weakly declined slope has increased the soil profile depth and the amount of fine textured soils towards the lower parts. According to the world reference data base for soil resources (*WRB)* the soils refer to Cambisols, Luvisols, Planosols, and Stagnosols *(IUSS Working Group WRB, 2007)*.

2.2 Leaf area index measurements

Thirty multispectral RapidEye images (Krischke et al., 2000) covering the years 2011 and 2012 were provided as geo- and atmospheric corrected level 3A products for the field site. Every image was locally geo-referenced on aerial images with a ground resolution of 0.4 m and subsequently converted into a raster of *LAI* (Ali et al., 2014). Therefore, the soil-adjusted vegetation index (*SAVI*) was calculated from the red-edge band (*RED*, 690-730 nm) and near infrared spectral band (*NIR*, 690-730 nm) according to Huete (1988):

$$SAVI = 1 + L\left[\frac{NIR - RED}{(NIR + RED) + L}\right], \tag{1}$$

where the soil brightness correction factor L was set to 0.5 (Aubin et al., 2000). The fractional vegetation cover (*FVC*) was computed according to Zeng et al. (2000):

$$FVC = \left[\frac{SAVI - SAVI_{soil}}{SAVI_{vegetation} - SAVI_{soil}} \right], \tag{2}$$

where $SAVI_{soil}$ and $SAVI_{vegetation}$ are the *SAVI* values calculated for bare soil and full vegetation cover, respectively. The final *LAI* was calculated using the formulation of Norman et al. (1995):

$$LAI = \frac{-\ln\left(1 - FVC\right)}{k\left(\theta\right)}, \tag{3}$$

where the light extinction coefficient $k(\theta)$ was set to 0.54. *LAI* data from RapidEye images were validated for the year 2012 by Ali et al. (2014) using on-ground *LAI* measurements of Stadler et al. (2014).

2.3 EMI measurements

Measurements of *ECa* were performed using the *CMD*-MiniExplorer (GFinstruments, Brno, Czech Republic). The sensor consists of three receiver coils separated by 0.32, 0.71, and 1.18 m from the transmitter coil resulting in a theoretical depth of exploration (*DOE*) of 0.25, 0.5, and 0.9 m in the vertical coplanar (*VCP*) and 0.5, 1.1, and 1.9 m for the horizontal coplanar (*HCP*) mode, respectively. To characterize the shallow subsurface, the *VCP* mode was used at all fields, whereas additional *HCP* measurements were taken at four selected fields (F01, F02, F07, and F10). The multi-receiver *EMI* sensor was mounted on a wooden sledge, connected to a *LEA-5T GPS* module (u-blox, Thalwil, Swiss), and pulled by an all-terrain vehicle (*ATV*) along parallel transects at approximately constant speed. Because of the presence of haystacks at F05, a lysimeter facility at F09, and an experimental setup consisting of a metal grid at F10, *ECa* could not be mapped over the entire fields. Due to restrictions in field management and crop rotation, *EMI* measurements were performed after harvest in summer 2012 and 2013 and measurements at fields F07, F08, and F09 could be repeated.

Geo-referenced *EMI*-readings were post-processed and corrected to a reference temperature of 25 °C (Corwin and Lesch, 2005) using soil temperature at a soil depth of 0.1 m measured by a weather station located at F10 by:

$$EC_{25} = f_t ECa \qquad f_t = 0.447 + 1.4034^{-T/26.815}, \tag{4}$$

where f_t is a temperature conversion factor and *T* the actual soil temperature [°C].

2.4 *ERT* measurements and *EMI* calibration

ERT measurements were performed along 30 m long transects perpendicular to prominent *ECa* patterns using the Syscal Pro (*IRIS* Instruments, Orleans, France) with a Dipole-Dipole array consisting of 120 electrodes with 0.25 m electrode spacing. The *ERT* measurements were post-processed using the automatic filtering procedure of Prosys II (IRIS Instruments, Orleans, France) and inverted by the robust inversion method of *RES2DINV* (Geotomo Software Sdn. Bhd., Penang, Malaysia) resulting in a horizontal and vertical conductivity distribution.

Although the CMD-MiniExplorer has been factory calibrated, negative *ECa* values were measured occasionally, and therefore, *ECa* data were calibrated using electrical resistivity tomography to obtain quantitative *ECa* values. At each position along the transect conductivity variations over depth were used as input in an electromagnetic forward model that assumes a horizontally layered medium, and *ECa* values were calculated using the pertaining offset, frequency, and configuration of respective *EMI* measurements. Finally, measured *EMI* data were calibrated using the linear regression approach as described by Lavoué et al. (2010) and von Hebel et al. (2014).

3. Results and discussion

3.1 LAI data

By the inspection of the 30 *LAI* maps estimated by RapidEye images (2011 and 2012), only for three dates at the end of a long lasting drought period (end of May 2011, see Fig. 1) distinctly different *LAI* characteristics in the study area could be observed (see Fig. 2). Figure 2a shows *LAI* patterns over an area of about 430 ha, which can be separated in roughly two zones due to different underlying parent material. In the southwest and northeast, the floodplain deposits of the Lower Terrace contains fields with relatively homogeneous and high *LAI* values (4-8 m^2 m^{-2}), whereas the sand and gravel dominated Upper Terrace contains generally lower *LAI* (0-4 m^2 m^{-2}) and crosses the study area from south-east to north-west as a prominent narrow band (length of 5.5 km and width up to 0.8 km). The boundary between the *LT* and *UT* is indicated by a dotted lines and is similar to the work of (Klostermann, 1992).

Figure 2b shows the area within the rectangle in Fig. 2a in more detail and a high number of slight to moderate undulating small-scale patterns of increased *LAI* values can be identified in the Upper Terrace deposits. Further analysis showed that the extent and appearance of the irregular *LAI* patterns was more pronounced in fields with cereal crops, which suggests a larger impact of water stress on these crops for the corresponding growing stage. A large variety of crop species grown in relatively small sized fields (< 2 ha) complicated the detection of further *LAI* anomalies.

Table 1 summarizes the mean *LAI* and corresponding standard deviation for fields F01-F10. In general, low *LAI* values with low standard deviations were found at the Upper Terrace (F01-F06). Higher *LAI* values that indicate better growth performance were measured along the weakly declined slope at the western part of the study area, especially at the Lower Terrace part of F07 (3.69±0.99) and F08 (2.53±1.26). An abrupt decrease in *LAI* values in the eastern part of fields F07, F08, and F09 and in the western part of field F02 indicate the transition of *LT* deposits towards coarse *UT* deposits (see Fig. 2b). Consequently, these fields are characterized by a higher standard deviation. The comparable low *LAI* values at F09 (1.52±0.77) are the result of a late sowing date accompanied by delayed plant emergence. In the following, the *LAI* values of F10 are withdrawn from the statistical analysis because this field was managed as bare soil.

3.2 EMI data

The quantitative *ECa* measurements (expressed as *ECa* hereafter) showed a distinct skewness and had to be log-transformed (Webster et al., 1994) to estimate experimental variograms. *ECa* measurements were field wise interpolated on a 0.25 x 0.25 m raster by ordinary kriging using the geostatistical library *GSLIB* (Deutsch and Journel, 1992). Figure 3a shows the quantitative *VCP2* data for all fields, where generally low *ECa* values were measured at fields (F01-F06) located above the gravel and sand dominated deposits, whereas more conductive soils with a higher *ECa* variability (see Tab. 1) were mapped in the western part. Despite the fact that fields were surveyed within two consecutive years (2012 and 2013), and therefore, under contrasting environmental conditions the *ECa* data are in reasonable agreement with the pedological map of Röhrig (1996). Deviations for the *LT/UT* boundary were visible at field F07. In addition, the *EMI* survey revealed different vertical *ECa* characteristics between both quaternary units. For the *UT* deposits a decrease of *ECa* measurements with depth implies shallow loamy soils over a thick terrace body of low conductive gravel material and, in consequence, a lower water holding capacity. In contrast, higher *ECa* values of the *LT* deposits were interpreted as increase of clay and related water content with depth. These assumptions were validated by drilling two geological boreholes at both ends of F09 which revealed shallow soils (< 0.5 m) above *UT* deposits reaching depths of > 4 m whereas at the higher conductive parts up to 3 m of fine textured soil were accumulated above the *LT* sediments. Repeated *ECa* measurements at F07, F08, and F09 (data shown in Stadler et al. (2014)) indicated time consistent *ECa* patterns with constant variability which emphasize the existence of a texture-driven systems according to Sudduth et al. (2001).

To investigate the within-field variability and remove the influence of any contrasting environmental condition and/or different agricultural management, the interpolated *ECa* field data were transformed to a standard *Z*-scale with zero mean and unit variance using:

$$ECa_Z = \frac{ECa - \mu_{ECa}}{\sigma_{ECa}}, \tag{5}$$

where ECa_Z is the *Z*-score of *ECa*, and μ_{ECa} and σ_{ECa} are the mean and standard deviation of *ECa*, respectively. Figure 3b shows the obtained normalized electrical conductivity data that clearly illustrate the within-field variability of F01-F06. Especially at F02 the boundary between the *UT* and *LT* sediments became more visible.

3.3 ECa versus LAI data

The comparison between *Z*-transformed *ECa* measurements in Figure 3b with *LAI* observations in Figure 2b of May 2011 showed almost identical patterns at F02, F07, F08, and F09 caused by the transition in parent material but also the narrow and curved patterns of better crop performance as indicated by the higher *LAI* values at F01, F02, and F05 were in coincidence with higher *ECa* values.

To enable a regression analysis between *ECa* and *LAI,* the interpolated *ECa* data were resampled to the coarser *LAI* image using the bilinear interpolation method in *R* (R Development Core Team, 2013). The higher conductive field borders at F02, F03, F04, and F06 showed no relation to *LAI* and were interpreted as zones affected by agricultural management. It is likely that these higher *ECa* values are a combined effect of soil compaction (Brevik and Fenton, 2004) and higher fertilization rates (Allred et al., 2003).To exclude those border effects, only the areas with 10 m distance from the field borders were considered for further analysis.

Figure 4 shows representative cross plots between the *LAI* and *ECa* measurements of summer 2012 for fields F01, F03 and F08 which obviously indicate differences between fields and pedological units. The highest relationship was found at F08 in March 2012 (R^2 = 0.82) using an exponential model. The exponential relationship can be related to the existence of two zones of crop development, whereby the area within the coarser and highly permeable *UT* deposits (0.3 ha in the eastern part of the field) are characterized by low *ECa* values and low water holding capacities resulting in a reduced crop development under water stress conditions. The other zone is characterized by *LT* deposits with deeper soil, which are more favorable for crop growth even during longer dry conditions. Although the *LT/UT* transition is also present at F02, F07, and F09 the contrast or the affected area was too small to result in an exponential tendency. A moderate to good linear relation between both parameters was found at F01 (R^2 = 0.23-0.46), F02 (R^2 = 0.32-0.47), F03 (R^2 = 0.50-0.56), F05 (R^2 = 0.28-0.36), F06 (R^2 = 0.32-0.41), F07 (R^2 = 0.48-0.66), and F09 (R^2 = 0.40-0.49) whereas the weakest correlation was obtained at F04 (R^2 = 0.19-0.21).A summary of the regression analysis for every field and *EMI* mode is given in Table 2.

3.4 Interpretation of ECa and LAI patterns using soil analysis

To quantify *EMI* and *LAI* patterns on soil texture and soil profile depth a soil survey was carried out in January 2013 at fields F01 and F02 showing narrow and undulating patterns as well as a transition in soil parent material. Soil texture (sand, silt, and clay) was analyzed in the lab according to *ISO 11277:2009* for each delineated horizon, whereby the material was taken from the augers. To regress soil properties on *ECa* and *LAI* respective measurements where extracted within a radius of 1 m around the sampling location (see Tab. 3). The spatial variability of soil profile depth in respect to *Z*-transformed *ECa* measurements is depicted in Figure 5, whereas a comparison of gravel content (fraction > 2 mm) as well topsoil and subsoil texture with *ECa* and *LAI* for F01 is given in Figure 6.

At both fields a high range in soil profile depth (0.3-2.0 m) was detected. For the 10 auger measurements at F02, a good statistical relationship between *ECa* and soil profile depth was found (R^2 0.56-0.69), indicating deeper soils in higher conductivity areas (see Tab. 4). The abrupt transition in soil parent material as suggested by *LAI* and *ECa* measurements could be confirmed by soil description along the points P66-P65-P64 which showed an increase of soil depth from 0.5 to 1.7 m within 25 m. In contrast, for the 16 auger measurements at F01 only a low statistical relations (R^2 0.11-0.25) were found due to the presence of exceptionally deep soils (P09 and P16) in low conductivity areas. A similar tendency was found between soil profile depth and *LAI* showing an excellent relation (R^2 = 0.82) at F02 but only R^2 = 0.21 at F01.

Topsoil texture regressed on *ECa* showed at F01 a moderate relation for sand (R^2 < 0.33) but no relation for silt and clay, whereas at F02 the relationship between clay and *ECa* ranged between R^2 0.32-0.41. Due to the high variability of topsoil gravel content at F01 (8-23 %), the fine fraction (< 2 mm) was corrected on the coarse material taken from a sample volume of 10 l at each auger location. Accordingly, the statistical relation improved between *ECa* and silt content (R^2 = 0.42), *ECa* and clay content (R^2 = 0.34) as well as *LAI* and silt content (R^2 = 0.37) and *LAI* and clay content (R^2 = 0.41).

Because clay content increased at both fields towards deeper horizons by a factor of 2.3 and 3.4 the regression analysis was repeated using subsoil texture. Especially for deeper *ECa* measurements the relationship improved to R^2 0.68 at F01 and R^2 0.60 at F02 whereas the relation between *LAI* and clay content showed better results only in F01 ($R^2 = 0.58$). Subsoil sand as well as silt content showed almost no statistical relationship with *ECa* or *LAI* measurements ($R^2 < 0.2$).

In August 2013 another severe drought period affected sugar beet in the region and water stressed and unstressed areas could be clearly observed (see Fig. 6d). Drought unstressed regions of the western part of F01 were mapped by walking through the field and mapping the position with a *DGPS* system. A comparison of these stress resistant zones with the *LAI* data of 2011 and 2013 as well as the *EMI* survey of 2012 indicates spatial and temporal consistency of subsoil properties influencing plant performance especially under drought conditions (Fig. 6a-c). Note that the unstressed crop patterns are most consistent with the *HCP3* data that has a *DOE* of 1.9 m. Together with the increased correlations between large-offset *ECa* data and the subsoil clay content; this indicates that the subsoil texture is mainly responsible for the crop performance in drought periods.

3.5 Analysis of selected LAI patterns using a combined sensor approach

To investigate the depth origin of the *LAI* patterns in more detail and to make use of the large number of data gathered at F01 we focused our analysis along a 145 m long north-south transect crossing two prominent structures (see Fig. 6a-c). The shallow *VCP1* mode (*DOE* 0.2 m) revealed a relatively high conductivity and homogeneous topsoil (*CV* = 0.04, Tab. 3, Fig. 7a), which was confirmed by *ERT* (Fig. 7c), a constant topsoil depth (0-0.3 m), and a small range of topsoil sand (12-18 %), silt (52-63 %), and clay content (13-17 %). The *ECa* measurements with large *DOE* showed more heterogeneity with a similar shape as the *LAI* data. The low *LAI* and *ECa* values at P05 and P06 can be explained by the presence of a very shallow soil (< 0.36 m) with the highest gravel content (> 17 %) along the profile.

Above the first structure located between 15 and 40 m, *ECa* measurements revealed a higher conductivity subsoil, which was confirmed by *ERT* measurements that indicated an oval-shaped zone at the central part of the 30 m long transect below 0.6 m depth. Consistent with the higher *ECa* and *LAI* values, the soil profile depth increased to 1.5 m towards the center of the structure whereas a clay content of up to 35 % was measured in the deeper soil horizon. Redoximorphic patterns at P07 below 0.6 m further imply that the soil is periodically influenced by water. P08 was located in a low conductivity area and a compact horizon with 55 % sand and 26 % clay content at a depth of < 0.6 m limited soil analysis to 0.9 m. P09 represents with 1.8 m the second deepest soil along the transect and showed similar soil properties as P07 as well as indications of stagnant water below 0.6 m. At this location, the increase of clay content towards deeper horizons was less pronounced (< 26 %), which explains the smaller *LAI* and *ECa* values. From the interpolated *ECa* measurements, we interpreted P09 as part of a narrow structure, such as a filled gully, which did not affect plant growth significantly. Intermediate soil profile depths were found at P15 (0.8 m) and P14 (1 m). While clay content at P15 was homogeneous with depth (16 %) a dense sandy horizon (> 50 %), similar to P08, appeared below 0.6 m and could be traced towards P14 until 1 m depth where clay content increased up to 24 % in the subsoil. *LAI* and *ECa* measurements showed a similar positive response to the higher subsoil clay content. At P16 the soil was comparable to P09 but no indications of stagnant water could be found in deeper layers. These results indicate that an increased clay content and hence increased water storage capacity are responsible for the improved crop performance and higher *ECa* and higher *LAI* values are obtained. Based on these findings the structures were confirmed as segments of a buried paleo-river.

4. Conclusion

In this study, the origin of crop patterns in large scale multi-temporal satellite imagery were investigated using multi-receiver *EMI* data, selected *ERT* transects, and ground truth texture data. *LAI* estimations by RapidEye images, taken under severe drought conditions, revealed a distinct *LAI* variability at regional scale separating the study area in two distinct zones. Regular high amplitude *LAI* patterns could be observed above the Lower Terrace, whereas lower *LAI* values with undulating patterns of increased *LAI* values appeared above the Upper Terrace.

Generally, low *ECa* values were measured at *UT* fields (F01-F06) with shallow soils over gravel and sand dominated deposits, whereby deeper and more conductive soils with a higher *ECa* variability were mapped at the *LT* fields (F07-F10).

High resolution multi-receiver *EMI* measurements were able to reconstruct the lateral and vertical changes in soil apparent electrical conductivity which was confirmed by the *ERT* measurements and soil probes. The small-offset *EMI* data with a *DOI* of about 0.2 m indicated a relatively homogeneous top soil while measurements with intermediate and large *DOI* showed higher conductivity areas at local scale that correspond with higher *LAI* patterns irrespectively of the fact that the *EMI* surveys were not performed under drought conditions. Regression analysis revealed a moderate to excellent relationship (R^2 0.19-0.82) between *LAI* and *ECa* by fitting linear or exponential models.

At two selected fields, narrow zones with better plant performance, large *LAI* vales and increased *ECa* were analyzed in detail by *ERT* transects and auger samples. *ERT* results showed that the increased *EMI* data with larger *DOI* were due to the presence of an increased conductivity zone below 0.6 m depth and soil cores confirmed deeper soil with a significantly higher amount of clay in the subsoil. The fine textured sediments within coarser terrace deposits were interpreted as remnants of a buried paleo-channel system. The fine textured soil and the related higher water holding capacity along the buried river segments implied an increased amount of plant available water and hence better crop performance, especially under severe drought conditions. The obtained results show that crop-subsoil interaction of arable fields is responsible for the spatial and temporal variation of the crop performance, whereas the deeper subsoil up to 1.9 m depth has the main influence on the crop performance in drought periods as indicated by the large correlation between the *LAI* and *EMI* measurements with larger *DOI*.

Furthermore, auger samples confirmed that stagnant water occurs within these paleo-channels which indicate that these structures still play an important role in subsurface hydrology. Lateral water transport through these paleo-channels from the fields located at the *UT* to the areas located at the *LT* is indicated by the fact that an experimental trench (Weihermüller et al., 2013) located at the eastern part of field F09 was heavily flooded by infiltrating water from the side walls during winter 2011/2012, whereby up to 12,000 litres of drainage water were pumped out daily. More research is needed to investigate how the water is laterally and vertically translocated in the area and what this means for the water availability for crop growth at surrounding fields or locations including the risk assessment with respect to nitrogen and pesticide transport.

5. Acknowledgements

This study was supported by the Federal Ministry of Education and Research (Competence network for phenotyping science-CROP.SENSe.net), the German Research Foundation DFG (Transregional Collaborative Research Centre 32-Patterns in Soil-Vegetation-Atmosphere Systems: Monitoring, modeling and data assimilation), ‘TERrestrial ENvironmental Observatories’ (TERENO), and Advanced Remote Sensing-Ground-Truth Demo and Test Facilities (ACROSS). RapidEye data were provided by the RapidEye Science Archive (RESA).

6. References

Abdu, H., Robinson, D.a., Jones, S.B., 2007. Comparing bulk soil electrical conductivity determination using the DUALEM-1S and EM38-DD electromagnetic induction instruments. Soil Sci. Soc. Am. J. 71(1), 189-196.

Akbar, M.A., Kenimer, A.L., Searcy, S.W., 2004. Estimating soil profile depth with apparent electrical conductivity for a Texas Vertisol. T. ASAE 47(4), 1087-1092.

Ali, M., Montzka, C., Stadler, A., Menz, G., Vereecken, H., 2014. Estimation and validation of RapidEye based time series of Leaf Area Index for winter wheat in the Rur catchment, Germany. Remote Sensing, (submitted).

Allred, B., Ehsani, R., Daniels, J., 2003. The impact on electrical conductivity measurement due to soil profile properties, shallow hydrologic conditions, fertilizer application, agricultural tillage, and the type of geophysical method employed, 16th EGGS Symposium on the Application of Geophysics to Engineering and Environmental Problems, San Antonio, TX, pp. 336-349.

Altdorff, D., Dietrich, P., 2012. Combination of electromagnetic induction and gamma spectrometry using K-means clustering: A study for evaluation of site partitioning. Journal of Plant Nutrition and Soil Science 175(3), 345-354.

André, F., van Leeuwen, C., Saussez, S., Van Durmen, R., Bogaert, P., Moghadas, D., de Resseguier, L., Delvaux, B., Vereecken, H., Lambot, S., 2012. High-resolution imaging of a vineyard in south of France using ground-penetrating radar, electromagnetic induction and electrical resistivity tomography. J. Appl. Geophys. 78(SI), 113-122.

Aubin, I., Beaudet, M., Messier, C., 2000. Light extinction coefficients specific to the understory vegetation of the southern boreal forest, Quebec. Can J Forest Res 30(1), 168-177.

Ben-Dor, E., Chabrillat, S., Dematte, J.A.M., Taylor, G.R., Hill, J., Whiting, M.L., Sommer, S., 2009. Using imaging spectroscopy to study soil properties. Remote Sens. Environ. 113, S38-S55.

Besson, A., Cousin, I., Bourennane, H., Nicoullaud, B., Pasquier, C., Richard, G., Dorigny, A., King, D., 2010. The spatial and temporal organization of soil water at the field scale as described by electrical resistivity measurements. Eur. J. Soil Sci. 61(1), 120-132.

Brevik, E.C., Fenton, T.E., 2004. The effect of changes in bulk density on soil electrical conductivity as measured with the geonics EM-38. Soil Surv. Horiz. 45, 96-102.

Casa, R., Castaldi, F., Pascucci, S., Basso, B., Pignatti, S., 2013. Geophysical and hyperspectral data fusion techniques for in-field estimation of soil properties. Vadose Zone J. 12(4).

Castrignanò, A., Wong, M.T.F., Stelluti, M., De Benedetto, D., Sollitto, D., 2012. Use of EMI, gamma-ray emission and GPS height as multi-sensor data for soil characterisation. Geoderma 175-176, 78-89.

Corwin, D.L., 2008. Past, present, and future trends of soil electrical conductivity measurements using geophysical methods. In: B. Allred, J.J. Daniels, M.R. Ehsani (Eds.), Handbook of Agricultural Geophysics, pp. 17-44.

Corwin, D.L., Lesch, S.M., 2005. Apparent soil electrical conductivity measurements in agriculture. Comput. Electron. Agric. 46, 11-43.

De Benedetto, D., Castrignano, A., Rinaldi, M., Ruggieri, S., Santoro, F., Figorito, B., Gualano, S., Diacono, M., Tamborrino, R., 2013. An approach for delineating homogeneous zones by using multi-sensor data. Geoderma 199(SI), 117-127.

De Benedetto, D., Castrignanò, A., Sollitto, D., Modugno, F., Buttafuoco, G., lo Papa, G., 2012. Integrating geophysical and geostatistical techniques to map the spatial variation of clay. Geoderma 171-172(SI), 53-63.

De Smedt, P., Saey, T., Lehouck, A., Stichelbaut, B., Meerschman, E., Islam, M.M., De Vijver, E.V., Van Meirvenne, M., 2013. Exploring the potential of multi-receiver EMI survey for geoarchaeological prospection: A 90 ha dataset. Geoderma 199(SI), 30-36.

Deutsch, C.V., Journel, A.G., 1992. GSLIB—Geostatistical software library and user's guide. Oxford Univeristy Press.

Dierke, C., Werban, U., 2013. Relationships between gamma-ray data and soil properties at an agricultural test site. Geoderma 199(SI), 90-98.

Eisele, A., Lau, I., Hewson, R., Carter, D., Wheaton, B., Ong, C., Cudahy, T.J., Chabrillat, S., Kaufmann, H., 2012. Applicability of the thermal infrared spectral region for the prediction of soil properties across semi-arid agricultural landscapes. Remote Sens-Basel 4(11), 3265-3286.

Govender, M., Dye, P.J., Weiersbye, I.M., Witkowski, E.T.F., Ahmed, F., 2009. Review of commonly used remote sensing and ground-based technologies to measure plant water stress. Water Sa 35(5), 741-752.

Hendrickx, J.M.H., Kachanoski, R.G., 2002. Nonintrusive electromagnetic induction. In: J.H. Dane, Topp, G.C. (Ed.), Methods of soil analysis Part 4. SSSA Book Ser. 5. SSSA, Madison, WI, pp. 1297–1306.

Huete, A.R., 1988. A soil-adjusted vegetation index (SAVI). Remote Sens. Environ. 25(3), 295-309.

Huisman, J.A., Hubbard, S., Redman, J.D., Annan, A.P., 2003. Measuring soil water content with ground penetrating radar: A review. Vadose Zone J. 2(4), 476-491.

ISO, 2009. Soil quality: Determination of particle size distribution in mineral soil material; Method by sieving and sedimentation, ISO 11277:2009, Geneva: International Organization for Standardization.

IUSS Working Group WRB, 2007. World Reference Base for Soil Resources 2006, first update 2007. World Soil Resources Reports No. 103. FAO, Rome.

Jonard, F., Mahmoudzadeh, M., Roisin, C., Weihermuller, L., Andre, F., Minet, J., Vereecken, H., Lambot, S., 2013. Characterization of tillage effects on the spatial variation of soil properties using ground-penetrating radar and electromagnetic induction. Geoderma 207, 310-322.

Jonard, F., Weihermuller, L., Jadoon, K.Z., Schwank, M., Vereecken, H., Lambot, S., 2011. Mapping field-scale soil moisture with L-band radiometer and ground-penetrating radar over bare soil. IEEE Trans. Geosci. Remote Sens. 49(8), 2863-2875.

Jung, W.K., Kitchen, N.R., Sudduth, K.A., Kremer, R.J., Motavalli, P.P., 2005. Relationship of apparent soil electrical conductivity to claypan soil properties. Soil Sci. Soc. Am. J. 69, 285-308.

Kachanoski, R.G., Gregorisch, E.G., van Wesenbeeck, I.J., 1988. Estimating spatial variations of soil water content using noncontacting electromagnetic inductive methods. Can. J. Soil Sci. 68, 715-722.

Klostermann, J., 1992. Das Quartär der Niederrheinischen Bucht Geologisches Landesamt Nordrhein-Westfalen.

Krischke, M., Niemeyer, W., Scherer, S., 2000. RapidEye - Satellite based geo-information system. Acta Astronaut 46(2-6), 307-312.

Kruger, J., Franko, U., Fank, J., Stelzl, E., Dietrich, P., Pohle, M., Werban, U., 2013. Linking geophysics and soil function modeling - An application study for biomass production. Vadose Zone J. 12(4).

Lausch, A., Zacharias, S., Dierke, C., Pause, M., Kühn, I., Doktor, D., Werban, U., 2013. Analysis of vegetation and soil pattern using hyperspectral remote sensing , EMI and Gamma-ray measurements. Vadose Zone J. 12(4).

Lavoué, F., van der Kruk, J., Rings, J., André, F., Moghadas, D., Huisman, J.A., Lambot, S., Weihermüller, L., Vanderborght, J., Vereecken, H., 2010. Electromagnetic induction calibration using apparent electrical conductivity modelling based on electrical resistivity tomography. Near Surf. Geophys. 8(6), 553-561.

Lelong, C.C.D., Pinet, P.C., Poilve, H., 1998. Hyperspectral imaging and stress mapping in agriculture: A case study on wheat in Beauce (France). Remote Sens. Environ. 66(2), 179-191.

Lu, D.S., 2006. The potential and challenge of remote sensing-based biomass estimation. Int. J. Remote Sens. 27(7), 1297-1328.

Lück, E., Ruehlmann, J., Kirchmann, H., 2011. Properties of soils from the Swedish long-term fertility experiments: VI. Mapping soil electrical conductivity with different geophysical methods. Acta Agriculturae Scandinavica, Section B - Plant Soil Science 61(5), 438-447.

McBratney, A.B., Santos, M.L.M., Minasny, B., 2003. On digital soil mapping. Geoderma 117(1-2), 3-52.

McNeill, J.D., 1980. Electromagnetic terrain conductivity measurement at low induction numbers.

Mester, A., van der Kruk, J., Zimmerman, E., Vereecken, H., 2011. Quantitative two-layer conductivity inversion of multi-configuration electromagnetic induction measurements. Vadose Zone J. 10(4), 1319-1330.

Mohanty, B.P., Cosh, M., Lakshmi, V., Montzka, C., 2013. Remote sensing for vadose zone hydrology - A synthesis from the vantage point. Vadose Zone J. 12(3).

Norman, J.M., Kustas, W.P., Humes, K.S., 1995. Source approach for estimating soil and vegetation energy fluxes in observations of directional radiometric surface temperature. Agr. Forest Meteorol. 77, 263-293.

Pätzold, S., Mertens, F.M., Bornemann, L., Koleczek, B., Franke, J., Feilhauer, H., Welp, G., 2008. Soil heterogeneity at the field scale: a challenge for precision crop protection. Precis. Agric. 9(6), 367-390.

R Development Core Team, 2013. R: A language and environment for statistical computing, 1. Vienna.

Robinson, D.a., Abdu, H., Lebron, I., Jones, S.B., 2012. Imaging of hill-slope soil moisture wetting patterns in a semi-arid oak savanna catchment using time-lapse electromagnetic induction. J. Hydrol. 416-417, 39-49.

Robinson, D.A., Lebron, I., Querejeta, J.I., 2010. Determining soil–tree–grass relationships in a california oak savanna using eco-geophysics. Vadose Zone J. 9(3), 528.

Röhrig, W., 1996. Bodenkarte 1 : 5000 zur landwirtschaftlichen Standorterkundung (BK5L). Geologischen Landesamt Nordrhein-Westfalen, Krefeld.

Saey, T., de Smedt, P., Islam, M.M., Meerschman, E., van de Vijver, E., Lehouck, A., van Meirvenne, M., 2012. Depth slicing of multi-receiver EMI measurements to enhance the delineation of contrasting subsoil features. Geoderma 189-190, 514-521.

Saey, T., Simpson, D., Vermeersch, H., Cockx, L., Van Meirvenne, M., 2009. Comparing the EM38DD and DUALEM-21S sensors for depth-to-clay mapping. Soil Sci. Soc. Am. J. 73(1), 7-12.

Samouelian, a., Cousin, I., Tabbagh, a., Bruand, a., Richard, G., 2005. Electrical resistivity survey in soil science: A review. Soil Tillage Res. 83(2), 173-193.

Stadler, A., Rudolph, S., Kupisch, M., Langensiepen, M., van der Kruk, J., Ewert, F., 2014. Quantifying the effects of soil variability on crop growth using apparent soil electrical conductivity measurements. European Journal of Agronomy, (submitted).

Sudduth, K.A., Drummond, S.T., Kitchen, N.R., 2001. Accuracy issues in electromagnetic induction sensing of soil electrical conductivity for precision agriculture. Comput. Electron. Agric. 31(3), 239-264.

Triantafilis, J., Lesch, S.M., 2005. Mapping clay content variation using electromagnetic induction techniques. Comput. Electron. Agric. 46(1-3), 203-237.

Triantafilis, J., Roe, J.A.E., Monteiro Santos, F.A., 2011. Detecting a leachate plume in an aeolian sand landscape using a DUALEM-421 induction probe to measure electrical conductivity followed by inversion modelling. Soil Use and Management 27(3), 357-366.

Vandenberghe, J., van Overmeeren, R.A., 1999. Ground penetrating radar images of selected fluvial deposits in the Netherlands. Sediment. Geol. 128(3-4), 245-270.

Vereecken, H., Huisman, J.A., Bogena, H., Vanderborght, J., Vrugt, J.A., Hopmans, J.W., 2008. On the value of soil moisture measurements in vadose zone hydrology: A review. Water Resour. Res. 44.

Vereecken, H., Weihermuller, L., Jonard, F., Montzka, C., 2012. Characterization of crop canopies and water stress related phenomena using microwave remote sensing methods: A review. Vadose Zone J. 11(2).

von Hebel, C., Rudolph, S., Mester, A., Huisman, J.A., Kumbhar, P., Vereecken, H., van der Kruk, J., 2014. Three-dimensional imaging of subsurface structural patterns using quantitative large-scale multi-configuration electromagnetic induction data. Water Resour. Res. 50(3), 2732–2748.

Webster, R., Atteia, O., Dubois, J.P., 1994. Coregionalization of trace-metals in the soil in the Swiss Jura. Eur. J. Soil Sci. 45(2), 205-218.

Weihermüller, L., Huisman, J., Lambot, S., Herbst, M., Vereecken, H., 2007. Mapping the spatial variation of soil water content at the field scale with different ground penetrating radar techniques. J. Hydrol. 340(3-4), 205-216.

Weihermüller, L., Huisman, J.A., Hermes, N., Pickel, S., Vereecken, H., 2013. A new TDR multiplexing system for reliable electrical conductivity and soil water content measurements. Vadose Zone J. 12(2).

Zeng, X., Dickinson, R.E., Walker, A., Shaikh, M., 2000. Derivation and evaluation of global 1-km fractional vegetation cover data for land modeling. J Appl Meteorol Clim 39, 826-839.

Zheng, G., Moskal, L.M., 2009. Retrieving leaf area index (LAI) using remote sensing: theories, methods and sensors. Sensors-Basel 9(4), 2719-2745.

Zribi, M., Kotti, F., Lili-Chabaane, Z., Baghdadi, N., Ben Issa, N., Amri, R., Duchemin, B., Chehbouni, A., 2012. Soil texture estimation over a semiarid area using TerraSAR-X radar data. IEEE Geosci. Remote Sens. Lett. 9(3), 353-357.

Figure 1: Walter & Lieth climatic diagram of the study area showing climatic records of the year 2011 which was characterized by a remarkable deficit of precipitation in spring. In addition the date of RapidEye image acquisition is illustrated.

Figure 2: *LAI* converted RapidEye image taken at the end of a long lasting drought period in May 2011 (see also Fig. 1). a) *LAI* patterns at regional scale (430 ha) showing fields with relatively homogeneous high *LAI* values above the floodplain deposits of the lower terrace (*LT*) in the southwest and northeast, whereas the sand and gravel dominated Upper Terrace (*UT*) contains lower *LAI* values. b) *LAI* pattern at the field scale that show a high number of slight to moderate undulating small-scale patterns of increased *LAI* values above the Upper Terrace deposits indicating a network of buried paleo-channels. Fields F01-F10 were surveyed with *EMI* in 2012 and 2013 (see also Fig. 3).

Figure 3: a) Pedological map and overlying *ECa* (σ) measurements for the *VCP2* mode indicating gravel and sand dominated soils in the east by low conductivities whereas deeper soils with higher clay content in the west where characterized by higher conductivities. b) *Z*-transformed *ECa* measurements (*VCP2* mode) illustrating within-field heterogeneities of the subsurface. Zones with positive (σZ) values indicating areas with *ECa* values above the field average and vice versa.

Figure 4: Regression between *LAI* (Mai 2011) and *ECa* (Summer 2012) measured in *VCP2* mode at a) a field crossed by meander like patterns of *LAI* and *ECa* (F01), b) a field with higher *ECa* variability (F03), and c) a field with a dominant transition in the underlying parent material from coarse to fine textured soils (F08) as indicated by the dashed line separating *UT* from *LT* deposits.

Figure 5: *Z*-transformed *VCP2* measurements (σZ) at fields a) F01 and b) F02 were used to identify regions with strong lateral variation in *ECa* which were investigated in detail by a soil sampling survey in January 2013. Soil profile depth and soil texture information were field wise regressed on *ECa* and *LAI* on respective sampling points (see also Tab. 4).

Figure 6: Comparison of a) satellite derived *LAI* data of Mai 2011, b) *VCP2* and c) *HCP3* measurements from June 2012 at field F01. d) Shows water stressed (A and C) and unstressed sugar beet (B) in August 2013 visible from the west (see also camera footprint in a) - c)). Unfortunately, no RapidEye images were available at this time period. Unstressed regions of the western part were

mapped using a *DGPS* and overlain in a) - c). In addition, a) includes the topsoil gravel content, b) shows the topsoil texture corrected on gravel content (0-40 cm), and c) summarizes the texture of the deepest horizon at the soil survey location (January 2013). *LAI* and *ECa* were compared with information of the soil survey along a 145 m long transect as indicated by the solid line (see Fig. 7).

Figure 7: a) Comparison of *LAI* and multi-receiver *ECa* measurements along the transect (shown in Fig. 6) with fine texture corrected on the coarse material of the topsoil layer, b) description of soil horizon, and c) inverted vertical cross section of *EC* between P6 and P8 measured by *ERT*.

Table 1: Summary table of satellite derived *LAI* data (Mai 2011) and shallow *ECa* measurements (*VCP1*, *VCP2*, *VCP3*) from respective fields. Note that the fields were mapped under contrasting environmental conditions and therefore only the coefficient of variation (*CV*) should be used to compare the variability of *ECa* and *LAI* between fields.

Table 2: Results of the regression analysis between *ECa* and *LAI* showing the coefficient of determination (R^2) for respective *EMI* mode and field. *ECa* and *LAI* values where derived from interpolated raster and only the measurements with 10 m distance from the field borders were considered. Except of field F08 a linear model was used.

Table 3: Summary table of parameters obtained at the soil sampling locations at fields F01 and F02 (see also Fig. 5). *ECa* and *LAI* values where extracted from interpolated raster within a radius of 1 m around the sampling location.

Table 4: Results of the regression analysis showing the coefficient of determination (R^2) between *ECa*, *LAI*, and soil parameter taken at F01 and F02.

Field			LAI*		ECa VCP1		ECa VCP2		ECa VCP3		Date of EMI survey
ID	Area	Terrace	Mean ± SD	CV	Mean ± SD	CV	Mean ± SD	CV	Mean ± SD	CV	
F01	2.77	UT	1.19 (± 0.44)	0.37	10.96 (± 0.65)	0.06	7.30 (± 0.98)	0.13	7.24 (± 1.09)	0.15	24/07/2012[a,b]
F02	3.04	LT/UT	1.35 (± 0.78)	0.58	12.28 (± 1.40)	0.11	9.64 (± 2.41)	0.25	9.96 (± 2.65)	0.27	25/07/2012[a]
F03	2.37	UT	0.98 (± 0.45)	0.46	9.24 (± 1.19)	0.13	7.06 (± 1.54)	0.22	9.08 (± 1.53)	0.17	03/08/2012[a,b]
F04	2.91	UT	1.14 (± 0.41)	0.36	11.65 (± 1.03)	0.09	7.76 (± 1.54)	0.20	8.95 (± 1.57)	0.18	03/08/2012[a]
F05	1.92	UT	1.24 (± 0.58)	0.47	7.20 (± 0.73)	0.10	3.09 (± 0.80)	0.26	5.15 (± 0.88)	0.17	08/08/2013[a]
F06	1.04	UT	1.26 (± 0.63)	0.50	9.21 (± 1.00)	0.11	6.87 (± 1.83)	0.27	8.21 (± 2.20)	0.27	08/08/2012[a]
F07	1.59	LT/UT	3.69 (± 0.99)	0.27	18.97 (± 3.34)	0.18	22.22 (± 5.74)	0.26	27.66 (± 6.51)	0.24	15/03/2012[a]
F07					7.83 (± 1.18)	0.15	8.07 (± 2.14)	0.27	12.09 (± 2.62)	0.22	13/09/2012[b]
F07					7.45 (± 1.09)	0.15	7.82 (± 2.37)	0.30	11.94 (± 3.08)	0.26	08/08/2013
F08	1.76	LT/UT	2.53 (± 1.26)	0.50	20.24 (± 3.47)	0.17	21.94 (± 6.10)	0.28	25.67 (± 7.27)	0.28	15/03/2012[a]
F08					6.85 (± 1.40)	0.20	7.09 (± 2.75)	0.39	11.53 (± 3.61)	0.31	13/09/2012
F09	0.78	LT/UT	1.52 (± 0.77)	0.51	18.12 (± 3.95)	0.22	20.21 (± 8.12)	0.40	23.95 (± 8.80)	0.37	15/03/2012[a]
F09					16.04 (± 3.96)	0.25	17.91 (± 7.09)	0.40	20.79 (± 7.62)	0.37	03/08/2012[a]
F09					10.47 (± 2.61)	0.25	13.23 (± 5.37)	0.41	17.47 (± 6.43)	0.37	08/08/2013
F10	1.14	LT/UT			12.95 (± 2.07)	0.16	12.75 (± 4.44)	0.35	14.52 (± 5.56)	0.38	29/06/2012[a]

[a] EMI measurements illustrated in Fig. 3 [b] EMI measurements illustrated in Fig. 4 * RapidEye acquisition from 30.05.2011

UT: Upper Terrace LT: Lower Terrace

Field	Terrace	R² between LAI and respective EMI mode						Date of EMI survey
		VCP1	VCP2	VCP3	HCP1	HCP2	HCP3	
F01	UT	0.23	0.37	0.39	0.36	0.43	0.46	24/07/2012
F02	LT/UT	0.32	0.37	0.39	0.38	0.42	0.47	25/07/2012
F03	UT	0.56	0.54	0.50				03/08/2012
F04	UT	0.19	0.19	0.21				03/08/2012
F05	UT	0.34	0.36	0.28				08/08/2013
F06	UT	0.41	0.37	0.32				08/08/2012
F07	LT/UT	0.48	0.63	0.64				15/03/2012
F07		0.21	0.54	0.63	0.61	0.66	0.63	13/09/2012
F07		0.48	0.64	0.64				08/08/2013
F08	LT/UT	0.72*	0.78*	0.82*				15/03/2012
F08		0.59	0.69*	0.53*				13/09/2012
F09	LT/UT	0.40	0.40	0.44				15/03/2012
F09		0.42	0.41	0.43				03/08/2012
F09		0.49	0.44	0.45				08/08/2013

* Exponential fit UT: Upper Terrace LT: Lower Terrace

		ECa [mS m^{-1}]						LAI	Depth	Gravel	Clay content [%]	
ID	Field	VCP1	VCP2	VCP3	HCP1	HCP2	HCP3	[-]	[m]	[%]	Topsoil	Subsoil
P01	F01	11.04	6.61	6.12	8.74	3.56	3.18	0.89	0.40	14.50	14.79	10.14
P02	F01	11.51	9.01	9.50	10.05	6.84	7.87	2.38	1.00	7.92	15.30	27.59
P03	F01	10.35	6.53	6.38	6.93	3.57	3.96	1.18	1.00	15.19	16.23	26.07
P04	F01	12.58	9.47	9.37	10.59	7.23	7.75	2.24	1.55	10.68	15.08	29.21
P05*	F01	10.17	5.85	5.61	5.66	1.82	1.46	0.50	0.30	22.72	13.19	16.93
P06*	F01	10.01	6.02	5.81	6.24	2.24	2.09	0.63	0.35	17.35	15.20	16.00
P07*	F01	11.71	9.50	10.14	10.07	7.46	8.35	1.93	1.50	11.23	15.29	35.23
P08*	F01	10.57	7.08	7.29	7.56	4.12	4.22	1.29	0.90	15.12	15.47	26.44
P09*	F01	10.34	6.59	6.41	7.16	3.86	4.11	1.11	1.80	12.03	13.40	25.54
P10	F01	11.18	9.06	9.93	9.95	8.11	9.01	2.27	1.50	12.22	15.44	39.60
P11	F01	11.61	8.46	8.45	8.62	5.77	6.11	1.17	1.00	10.59	15.10	22.70
P12	F01	11.30	8.79	9.42	7.12	3.96	4.82	1.78	1.00	8.66	14.36	29.53
P13	F01	11.11	8.05	8.64	7.43	4.25	4.56	1.73	1.00	7.90	17.23	19.89
P14*	F01	11.48	8.71	9.07	8.94	4.44	4.70	1.60	1.00	11.51	14.66	23.71
P15*	F01	10.22	5.88	5.55	6.00	1.75	1.51	0.97	0.80	12.85	14.68	16.16
P16*	F01	10.50	6.67	6.52	6.38	3.05	3.08	0.96	2.00	14.79	14.16	22.64
P56	F02	11.80	8.42	8.33	9.62	4.46	5.29	0.48	0.55		14.21	15.03
P57	F02	12.29	9.30	9.57	10.16	5.18	6.37	0.70	0.60		15.00	16.05
P58	F02	13.86	12.16	12.22	13.81	10.00	11.24	1.40	1.45		15.29	27.93
P61	F02	13.83	12.21	12.59	14.47	11.71	12.71	1.80	1.55		14.46	18.73
P62	F02	14.87	12.82	14.08	14.47	11.69	13.84	1.70	1.95		14.93	34.31
P64	F02	13.99	12.99	13.77	13.49	10.33	11.77	2.15	1.70		15.60	16.09
P65	F02	12.71	10.12	10.64	11.02	7.22	8.40	1.20	1.00		15.81	18.92
P67	F02	9.65	5.03	4.91	5.71	0.61	1.39	0.68	1.00		13.64	10.57

[*] Soil sampling location along the 145 long transect at F01

	Field	LAI	Soil depth	Topsoil							Subsoil		
				Gravel	Sand	Silt	Clay	Sand adj.	Silt adj.	Clay adj.	Sand	Silt	Clay
VCP1	F01	0.61	0.11	0.43	0.14	0.04	0.06	0.00	0.32	0.23	0.00	0.02	0.23
VCP2	F01	0.82	0.17	0.53	0.26	0.05	0.10	0.01	0.40	0.31	0.04	0.00	0.53
VCP3	F01	0.84	0.16	0.53	0.32	0.06	0.12	0.03	0.42	0.34	0.05	0.00	0.59
HCP1	F01	0.67	0.11	0.32	0.07	0.00	0.08	0.01	0.14	0.21	0.04	0.00	0.33
HCP2	F01	0.76	0.24	0.34	0.13	0.00	0.11	0.00	0.13	0.25	0.12	0.01	0.62
HCP3	F01	0.81	0.25	0.39	0.16	0.00	0.11	0.00	0.16	0.27	0.13	0.01	0.68
LAI	F01	1.00	0.21	0.58	0.35	0.02	0.17	0.04	0.37	0.41	0.05	0.00	0.58
Soil depth	F01	0.21	1.00	0.18	0.29	0.03	0.00	0.11	0.16	0.02	0.20	0.08	0.41
VCP1	F02	0.69	0.58	-	0.03	0.08	0.41	-	-	-	0.16	0.00	0.60
VCP2	F02	0.76	0.57	-	0.04	0.07	0.46	-	-	-	0.14	0.00	0.47
VCP3	F02	0.78	0.61	-	0.05	0.07	0.47	-	-	-	0.13	0.00	0.49
HCP1	F02	0.71	0.56	-	0.02	0.11	0.34	-	-	-	0.18	0.00	0.52
HCP2	F02	0.79	0.66	-	0.02	0.15	0.32	-	-	-	0.15	0.00	0.51
HCP3	F02	0.79	0.69	-	0.01	0.15	0.33	-	-	-	0.14	0.00	0.56
LAI	F02	1.00	0.82	-	0.00	0.21	0.27	-	-	-	0.01	0.03	0.21
Soil depth	F02	0.82	1.00	-	0.09	0.46	0.09	-	-	-	0.00	0.16	0.43

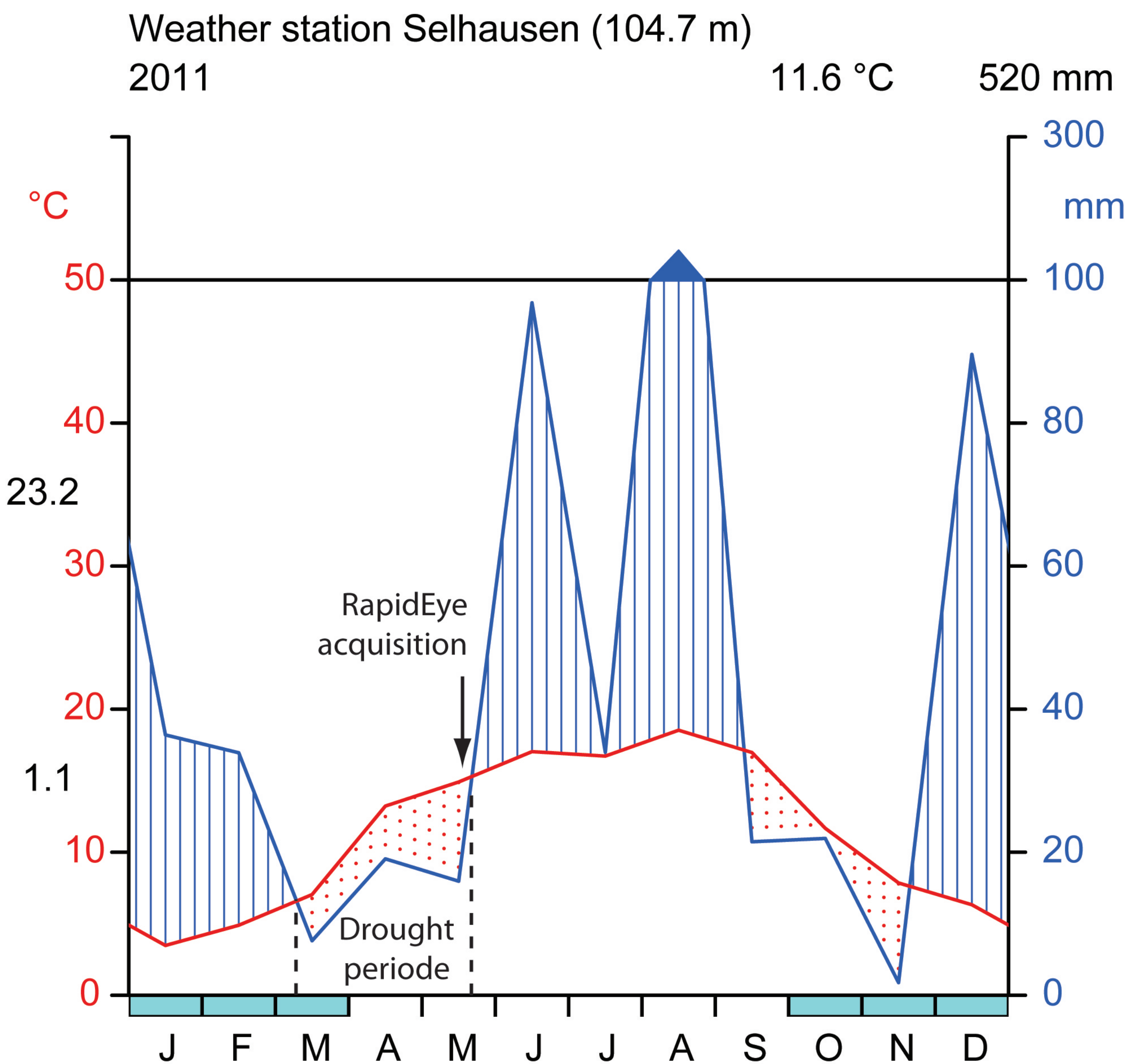

Weather station Selhausen (104.7 m)
2011
11.6 °C
520 mm
°C
mm
50
40
30
20
10
0
300
100
80
60
40
20
0
23.2
1.1
RapidEye acquisition
Drought periode
J
F
M
A
M
J
J
A
S
O
N
D

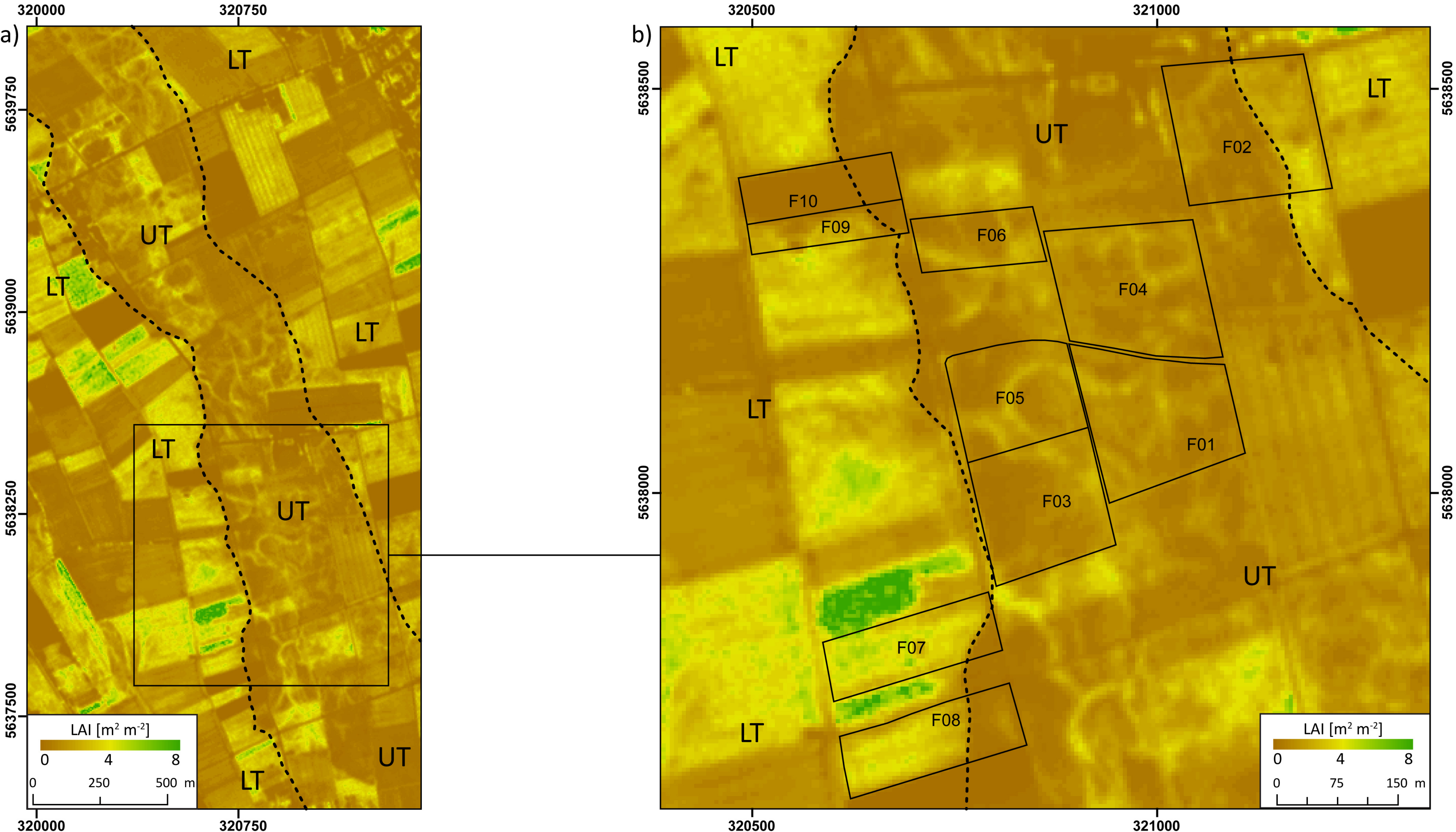

a)
320000
320750
5639750
5639000
5638250
5637500
LT
UT
LT
LT
LT
UT
LT
UT
LAI [m² m⁻²]
0
4
8
0
250
500
m
b)
320500
321000
5638500
5638000
LT
UT
LT
F02
F10
F09
F06
F04
LT
F05
F01
F03
UT
F07
F08
LT
LAI [m² m⁻²]
0
4
8
0
75
150
m

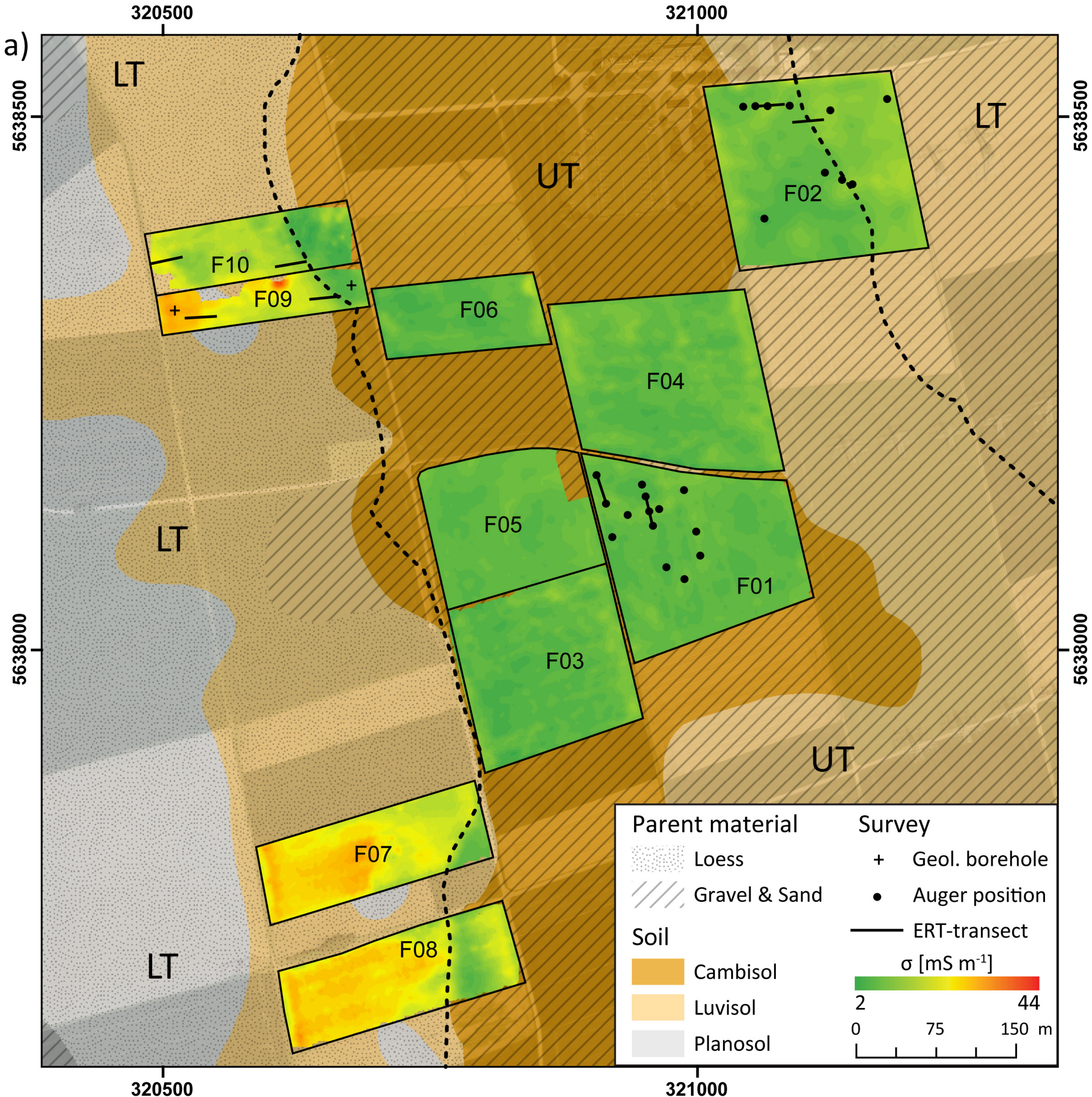
a)
320500
321000
5638500
5638000
LT
UT
LT
F02
F10
F09
F06
F04
F05
F01
F03
LT
UT
F07
F08
LT
Parent material
Loess
Gravel & Sand
Soil
Cambisol
Luvisol
Planosol
Survey
Geol. borehole
Auger position
ERT-transect
σ [mS m-1]
2
44
0
75
150 m

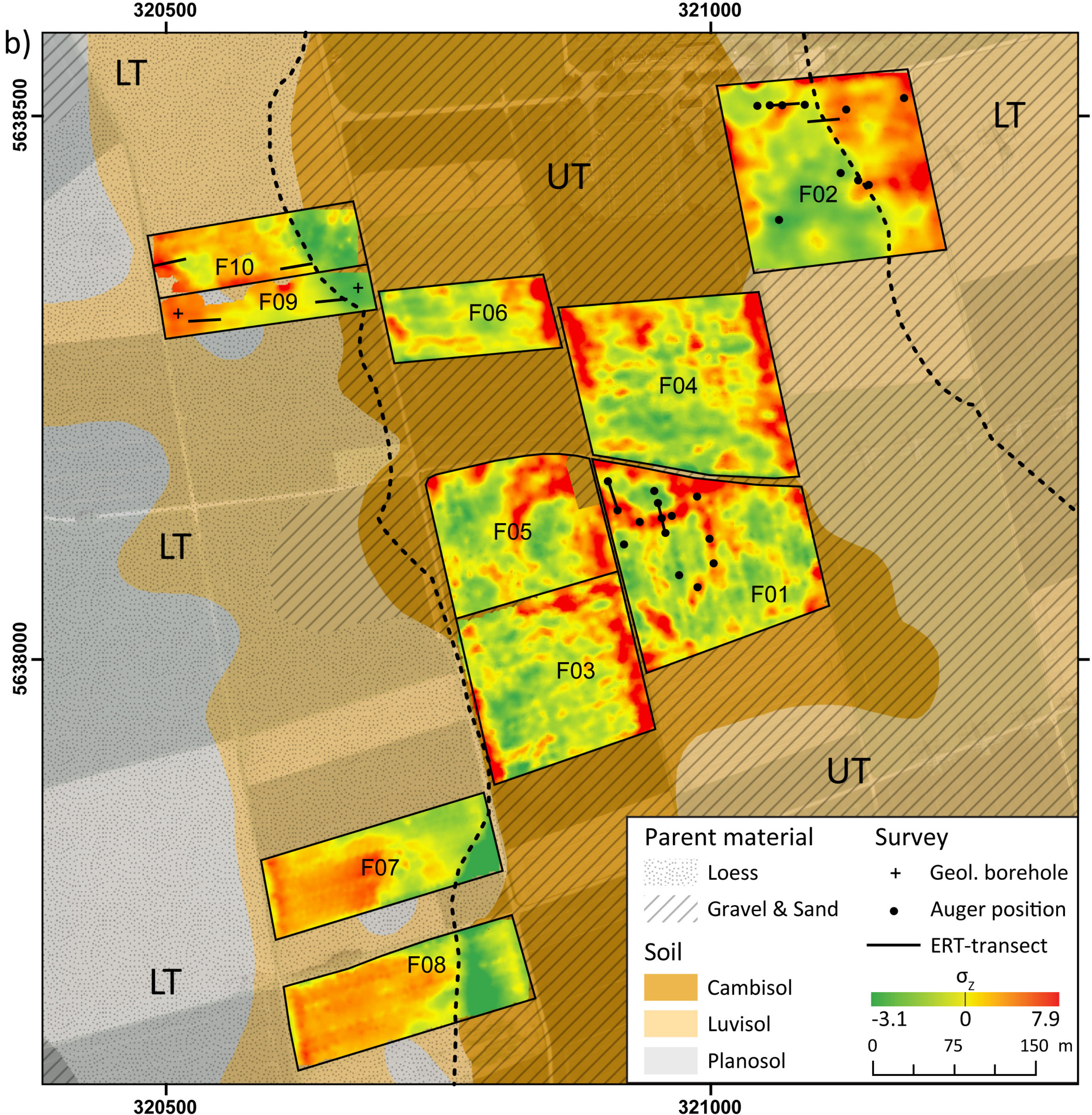
b)
320500
321000
5638500
5638000
LT
UT
LT
LT
UT
LT
F01
F02
F03
F04
F05
F06
F07
F08
F09
F10
Parent material
Loess
Gravel & Sand
Soil
Cambisol
Luvisol
Planosol
Survey
Geol. borehole
Auger position
ERT-transect
σz
-3.1
0
7.9
0
75
150
m

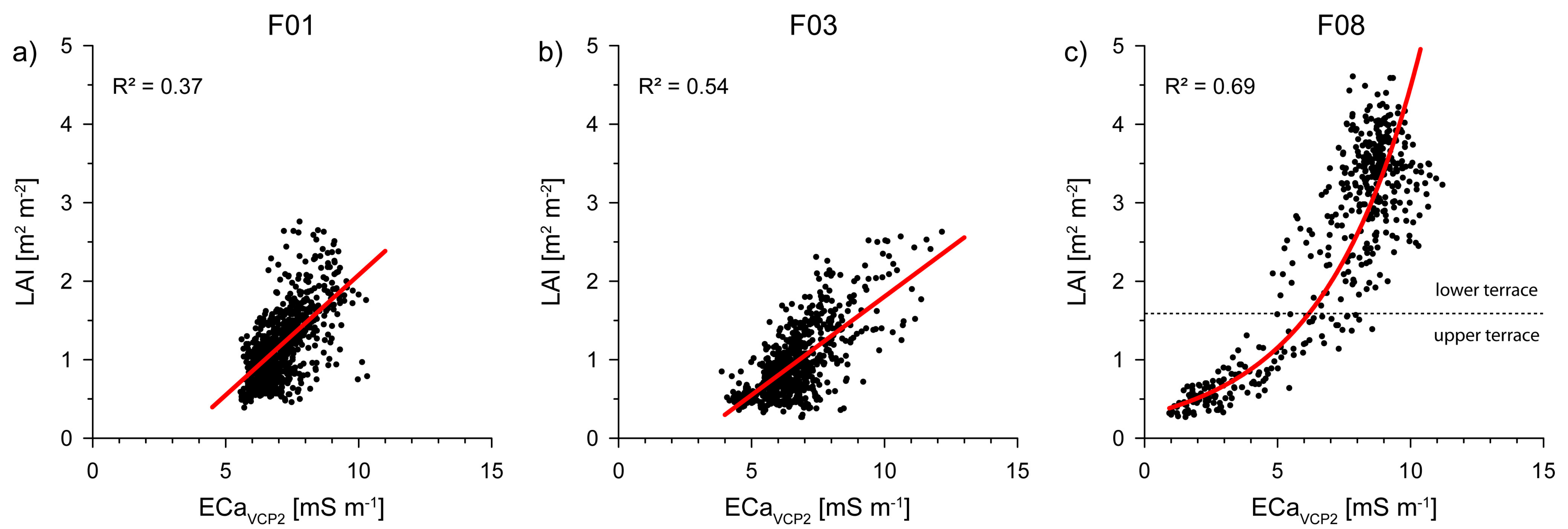
F01
a)
R² = 0.37
LAI [m² m⁻²]
ECa_VCP2 [mS m⁻¹]
F03
b)
R² = 0.54
LAI [m² m⁻²]
ECa_VCP2 [mS m⁻¹]
F08
c)
R² = 0.69
lower terrace
upper terrace
LAI [m² m⁻²]
ECa_VCP2 [mS m⁻¹]

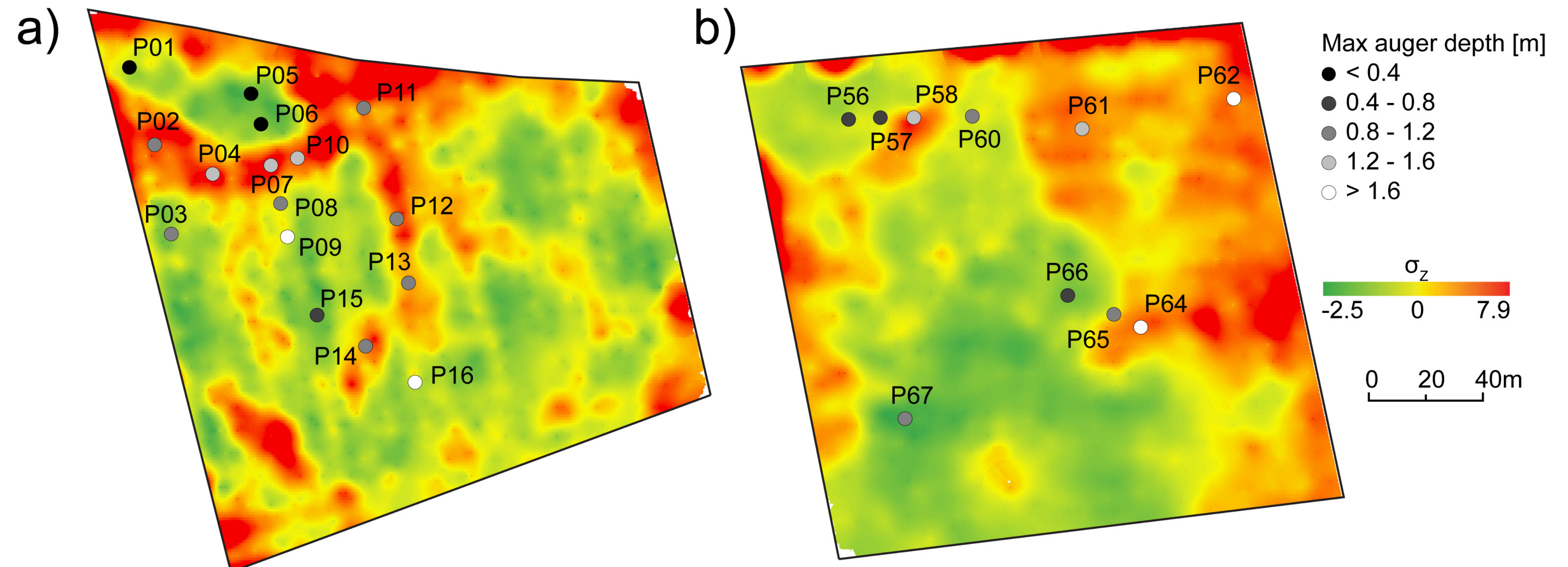
a)
P01
P02
P03
P04
P05
P06
P07
P08
P09
P10
P11
P12
P13
P14
P15
P16
b)
P56
P57
P58
P60
P61
P62
P64
P65
P66
P67
Max auger depth [m]
< 0.4
0.4 - 0.8
0.8 - 1.2
1.2 - 1.6
> 1.6
σz
-2.5
0
7.9
0
20
40m

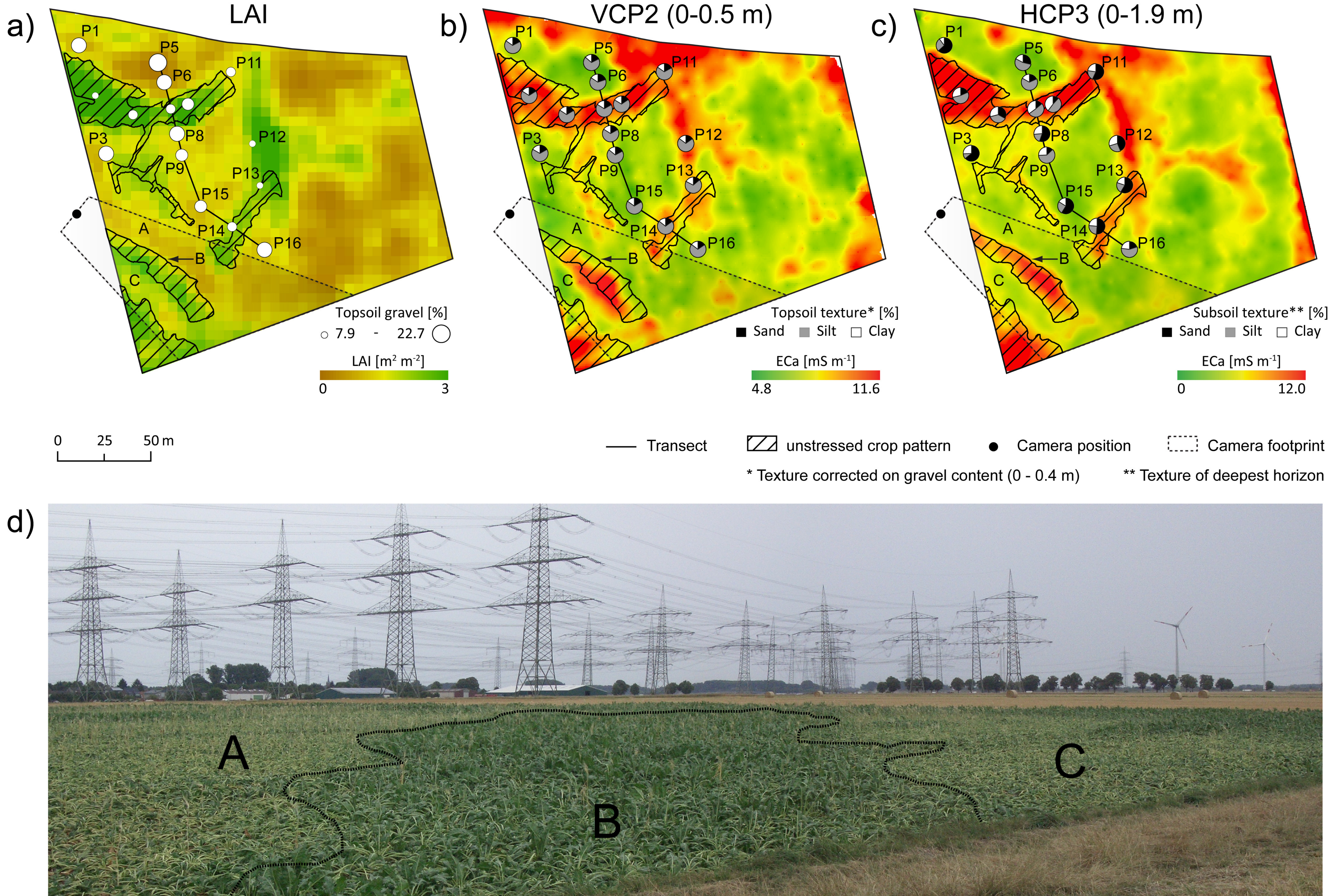
a)
LAI
P1
P5
P6
P11
P8
P12
P3
P9
P13
P15
P14
P16
A
B
C
Topsoil gravel [%]
7.9 - 22.7
LAI [m² m⁻²]
0
3
b)
VCP2 (0-0.5 m)
Topsoil texture* [%]
Sand
Silt
Clay
ECa [mS m⁻¹]
4.8
11.6
c)
HCP3 (0-1.9 m)
Subsoil texture** [%]
Sand
Silt
Clay
ECa [mS m⁻¹]
0
12.0
0
25
50 m
Transect
unstressed crop pattern
Camera position
Camera footprint
* Texture corrected on gravel content (0 - 0.4 m)
** Texture of deepest horizon
d)
A
B
C

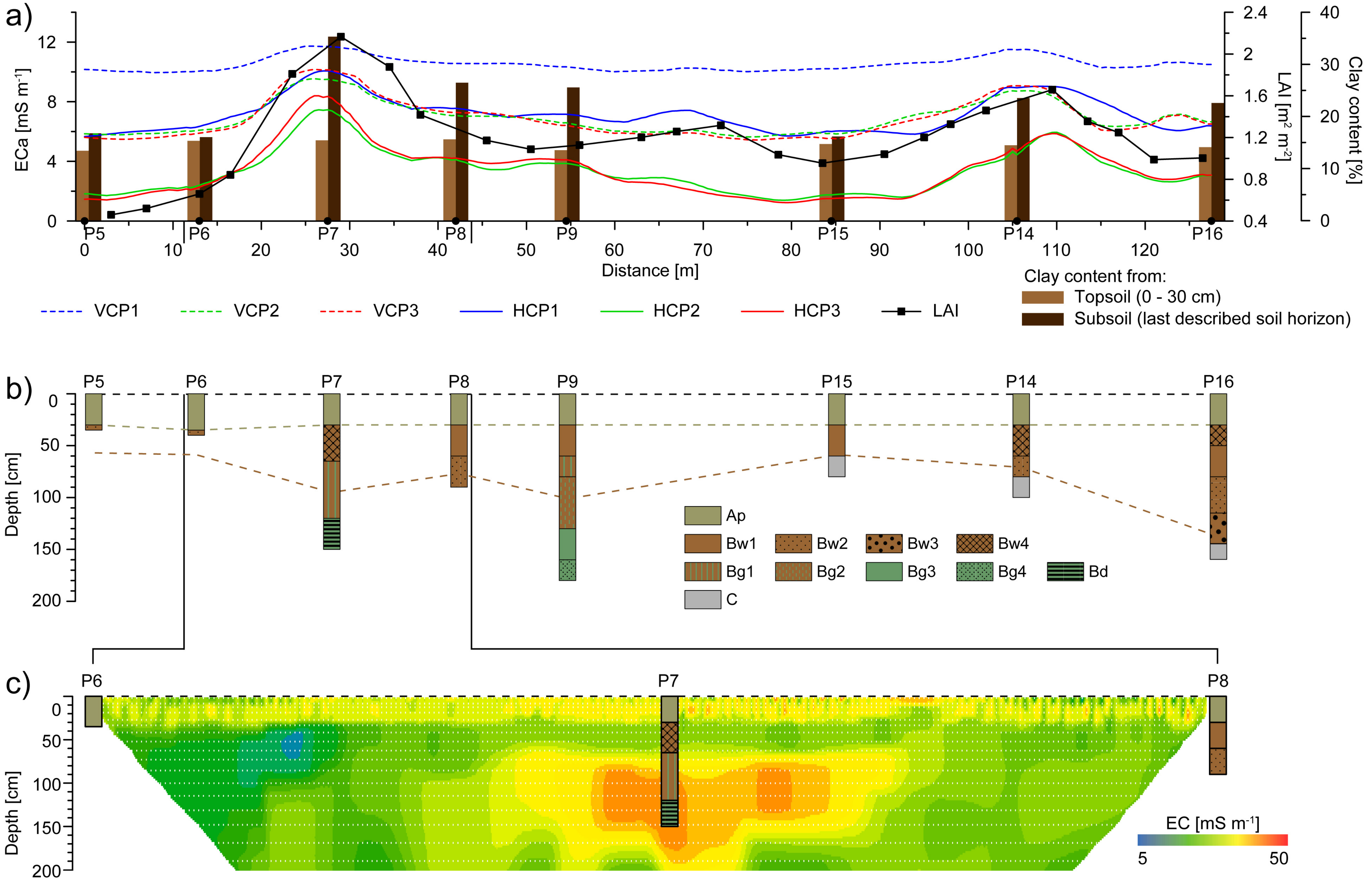

a)
ECa [mS m-1]
LAI [m2 m-2]
Clay content [%]
Distance [m]
P5
P6
P7
P8
P9
P15
P14
P16
VCP1
VCP2
VCP3
HCP1
HCP2
HCP3
LAI
Clay content from:
Topsoil (0 - 30 cm)
Subsoil (last described soil horizon)
b)
Depth [cm]
Ap
Bw1
Bw2
Bw3
Bw4
Bg1
Bg2
Bg3
Bg4
Bd
C
c)
EC [mS m-1]
5
50